ACS NANO

www.acsnano.org

ARTICLE

Defect-Mediated Faceted Lithium Nucleation on Carbon Composite Substrates

Sicen Yu, Xiaolu Yu, Sashank Shivakumar, Shen Wang, Erbin Qiu, Qiushi Miao, Junwei Gao, Min Wei, Jianbin Zhou, Zheng Chen, and Ping Liu*

Cite This: https://doi.org/10.1021/acsnano.4c03498

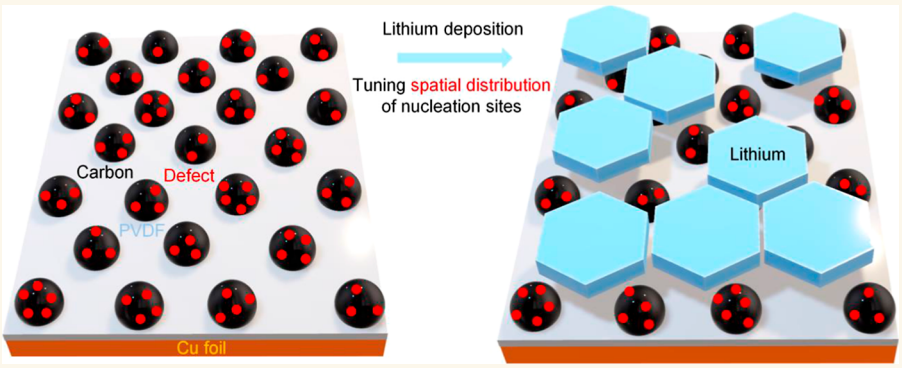

ABSTRACT: **The formation of uniform, nondendritic seeds is essential to realizing dense lithium (Li) metal anodes and long-life batteries. Here, we discover that faceted Li seeds with a hexagonal shape can be uniformly grown on carbon-polymer composite films. Our investigation reveals the critical role of carbon defects in serving as the nucleation sites for their formation. Tuning the density and spatial distribution of defects enables the optimization of conditions for faceted seed growth. Raman spectral results confirm that lithium nucleation indeed starts at the defect sites. The uniformly distributed crystalline seeds facilitate low-porosity Li deposition, effectively reducing Li pulverization during cycling and unlocking the fast-charging ability of Li metal batteries. At a 1 C rate, full cells using $LiNi_{0.8}Mn_{0.1}Co_{0.1}O_2$ cathode (4.5 mA h cm^{-2}) paired with a lithium anode grown on carbon composite films achieve a 313% improvement in cycle life compared to baseline cells. Polymer composites with carbonaceous materials rich in defects are scalable, low-cost substrates for high-rate, high-energy-density batteries.**

KEYWORDS: *lithium nucleation, spatial distribution of nucleation sites, carbon defects, faceted lithium, substrate*

INTRODUCTION

Li−metal batteries (LMBs) promise high theoretical energy density,[1,2] but still suffer from short cycle life due to the low reversibility and pulverization of electrodeposited Li.[3,4] Despite progress in electrolyte design that has improved the Coulombic efficiencies (CEs) of Li anodes to over 99.5%, further pushing up the value remains challenging.[5−9] Therefore, it is critical to develop a comprehensive understanding of the underlying mechanisms responsible for low-porosity Li electrodeposition, particularly during the initial stages, to ensure the effective maintenance of a low-porosity Li anode throughout the cycling process.

Li electrodeposition can be divided into two stages: nucleation and growth.[3] Various methods have been developed to reduce Li pulverization during growth, including the construction of a LiF-rich solid electrolyte interphase (SEI) layer,[10] utilization of 3D current collectors,[11] and the application of high pressure.[12,13] However, even under high pressure, the lower layer of electrodeposited Li near the substrate remains porous compared to the upper layer. On the other hand, faceted Li seeds formed during the nucleation stage have been shown to facilitate subsequent dense Li growth.[3] The formation of these seeds is enabled by a LiF-rich substrate on which rapid Li atomic transport is expected. Recent research suggests that pulsed electrodeposition at ultrahigh current densities (>100 mA cm^{-2}) promotes uniform

Received: March 13, 2024
Revised: May 26, 2024
Accepted: June 7, 2024

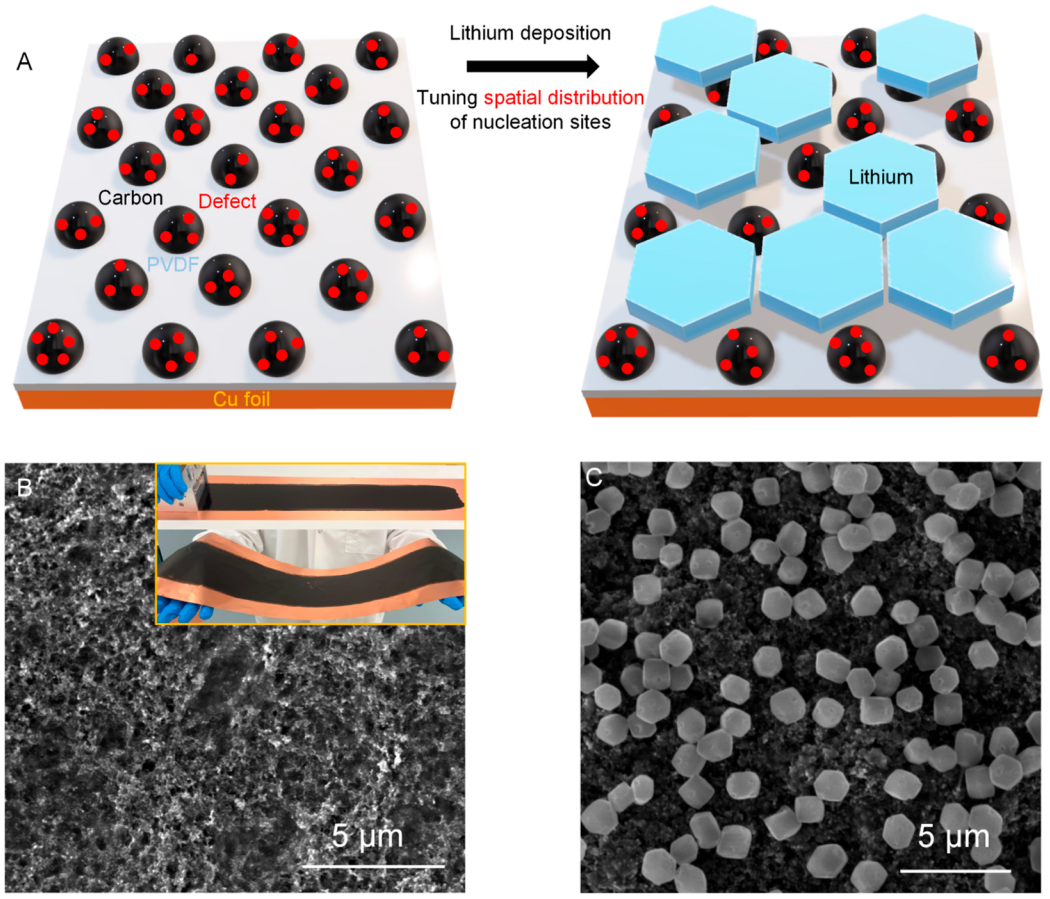

Figure 1. Electrodeposited faceted lithium crystals on carbon-polymer composite substrates. (A) Schematic diagrams of defect-mediated lithium deposition on carbon substrates. (B) SEM image of a carbon/polymer composite film (inset: optical image of blade cast film on copper); (C) SEM images of lithium crystals deposited on film shown in (B). Lithium is deposited at a constant current of 3 mA cm^{-2} and a capacity of 0.1 mA h cm^{-2}.

nucleation of faceted Li crystals.[14] Under these deposition conditions, Li growth apparently outpaces the formation of the SEI layer and is independent of the substrate. Utilizing a combined approach of pulsed electrodeposition for Li nucleation and continuous electrodeposition for Li growth yields improvements in Coulombic efficiency (CE).[15] However, the practicality of the pulsed electrodeposition strategy using these extreme parameters is questionable.

Substrates can also impact nucleation and have received increased attention. The general hypothesis is that the uniformity of energetically equivalent nucleation sites on the substrates determines the uniformity of the lithium nucleation and initial deposition. In this regard, commercial copper foil or lithium metal foil does not meet these requirements. They are inherently inhomogeneous due to the effects of processing or chemical contamination. A few strategies have been proposed to improve the uniformity. Cu current collectors with a $Cu_{99}Zn$ layer has been proposed where the dilute Zn atoms can react with Li and facilitate nucleation.[16] Recently, it was discovered that substrates coated with a lithiophobic nano-Fe/LiF coating can induce desirable faceted lithium nucleation. The in situ generated, uniformly distributed Fe nanoparticles serve as the nucleation sites while LiF facilitates Li surface transport.[3]

Despite these advancements, several fundamental questions remain. From a scientific perspective, what qualifies as a good nucleation site in terms of size and chemical/physical property? Is a strong interaction between the nucleation sites and Li necessary? How about the spatial distribution of nucleation sites? Although the Fe/LiF coating enables the formation of faceted crystals, there is not an easy way to tune the density and size of the nucleation sites. Zn forms alloys that appear to promote the formation of spherical lithium seeds, again with little control of the spatial distribution of nucleation sites. From a technological standpoint, are there substrates that are amenable to easy scaling up using existing battery manufacturing processes?

In this work, we report the fabrication of a carbon-polymer composite film to serve as a substrate to regulate the nucleation of lithium and facilitate the formation of uniform, faceted Li seeds (Figure 1A). We discover that the defects on the carbon particle surface serve as nucleation sites. The concentration and distribution of defects are readily tuned by choosing different carbon materials, through chemical or thermal treatments, and/or adjusting the carbon concentration in the composites. The interaction between the defects and lithium is directly probed by Raman spectroscopy. The carbon-polymer film can be deposited on copper by using a slurry casting process that is highly scalable. Implementation of this low-cost material promises to significantly improve the lithium nucleation process, leading to the formation of dense lithium layers that are essential for long-life lithium metal batteries.

https://doi.org/10.1021/acsnano.4c03498
ACS Nano XXXX, XXX, XXX−XXX

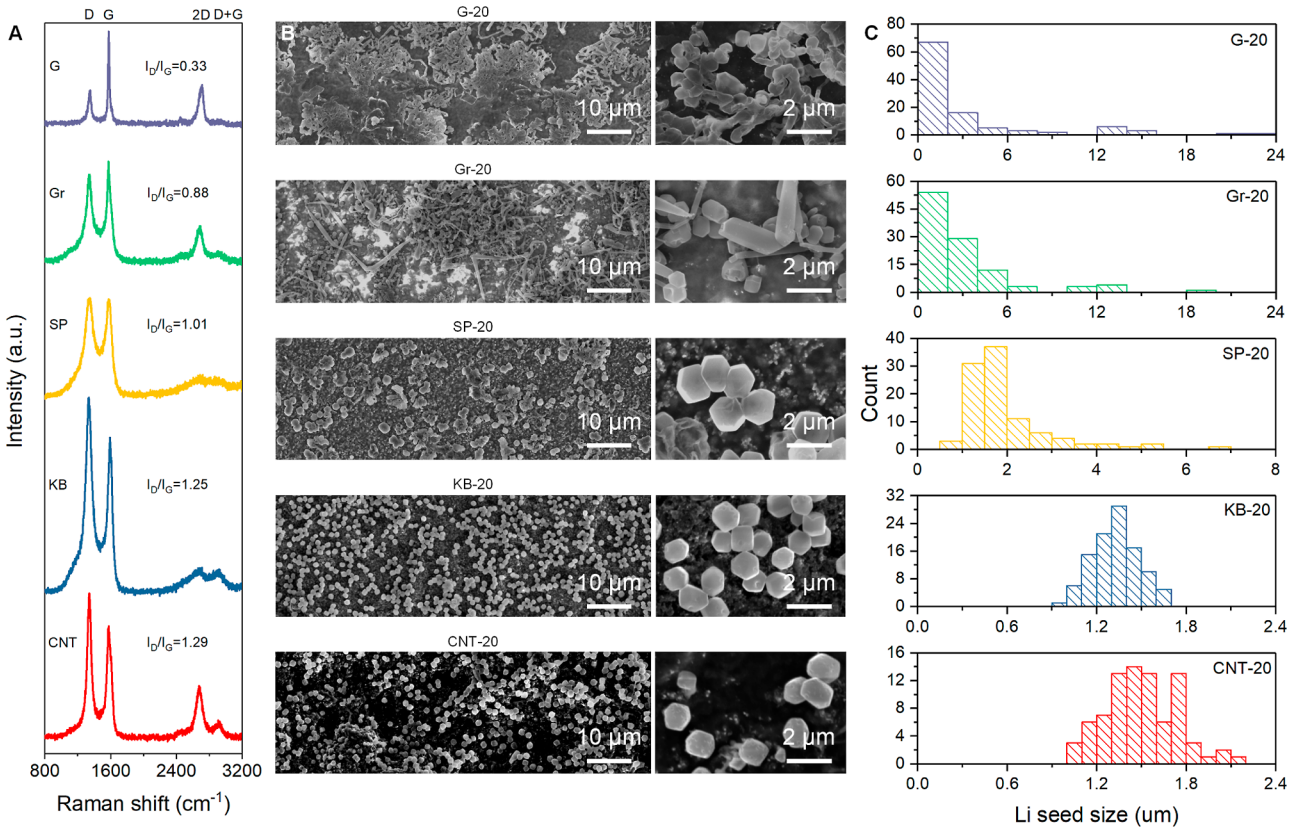

Figure 2. Effects of carbon on lithium nucleation. (A) Raman spectra of five carbon materials featuring different D band to G band intensity ratios or concentrations of defects; (B) SEM images of lithium nucleation on composite films containing different carbon materials; (C) size distribution of Li seeds shown in (B). Lithium is deposited at a constant current of 3 mA cm^{-2} and a capacity of 0.1 mA h cm^{-2}.

RESULTS AND DISCUSSION

Uniform Nucleation of Faceted Li Seeds on Carbon-Polymer Films. The carbon-polymer film is fabricated by a slurry casting method. The inset in Figure 1B shows an optical image of a large sheet of a film coated on copper. A typical carbon material is ketjen black (KB). The carbon is mixed with polyvinylidene fluoride (PVDF) in *N*-methyl-2-pyrrolidone (NMP), followed by casting and vacuum drying. The carbon-polymer film coated Cu foil is used as an electrode in a cell. The electrolyte is a localized high-concentration electrolyte, specifically 2 M lithium bis(fluorosulfonyl)imide (LiFSI) in 1,2-dimethoxyethane/bis(2,2,2-trifluoroethyl) ether (DME/BTFE) with a weight ratio of 1:4, which will be referred to as LDME. This electrolyte ensures a high CE for Li plating and stripping (>99%).[17] As a demonstration, we conduct an experiment in which 0.1 mA h cm^{-2} of Li is deposited on films at a current density of 3 mA cm^{-2}. Prior to deposition, the Lil carbon film cell is discharged to 0 V at a current density of 0.5 mA cm^{-2}. Figure 1C shows that hexagonally faceted Li seeds of similar sizes are uniformly distributed on the film. Adjusting the current density has an impact on the size of the seeds, with lower current densities resulting in larger crystals and higher current densities leading to smaller ones (Figure S1). Under the same conditions on bare copper in the same electrolyte, dendrites are formed (Figure S2). This phenomenon is further confirmed using a commercial carbonate electrolyte, 1.2 M lithium hexafluorophosphate ($LiPF_6$) in ethylene carbonate/ethyl methyl carbonate (EC/EMC in 3:7 wt %). Li deposited on the film also exhibits a hexagonal shape (Figure S3), suggesting that this phenomenon is primarily influenced by the presence of the carbon-polymer film rather than specific properties of the electrolytes. These hexagonally faceted crystals are likely single crystalline.[3] From a theoretical perspective, the hexagonal shape is considered to be the Wulff shape of Li due to the fact that the (110) plane has the lowest surface energy and the lowest surface diffusion barrier under battery working conditions.[18]

Lithium Nucleation on Different Carbon Materials and Its Correlation with Defects. To assess the impact of carbon on Li nucleation, we have studied five different types of carbon particles, namely, graphite (G), graphene (Gr), super P (SP), ketjen black (KB), and carbon nanotube (CNT), each possessing a distinct I_D/I_G ratio (0.33, 0.88, 1.01, 1.25, and 1.29, respectively), as depicted in the Raman spectra shown in Figure 2A. A higher I_D/I_G ratio indicates a higher concentration of carbon defects.[19] Intrinsic carbon defects primarily encompass edge and topological defects, which are accompanied by an abundance of unpaired π electrons.[20] These defects play a crucial role in facilitating efficient electron transfer processes and can serve as active sites for various reactions.[21] Additional characterizations of the carbon particles, such as morphology, XRD patterns, particle size, surface area, and wetting of molten Li on carbon, can be found in Figures S4–S7. Despite significant variation in apparent densities, the true densities of these carbon materials are quite similar (Table S1). The carbon-polymer films are referred to as C–W, where C denotes the carbon type (C: G, Gr, SP, KB, and CNT), and W represents the weight ratio of carbon in the film. In order to facilitate the assessment of the effect of carbon structure, all films shown in Figure 2 contain a fixed carbon

https://doi.org/10.1021/acsnano.4c03498
ACS Nano XXXX, XXX, XXX–XXX

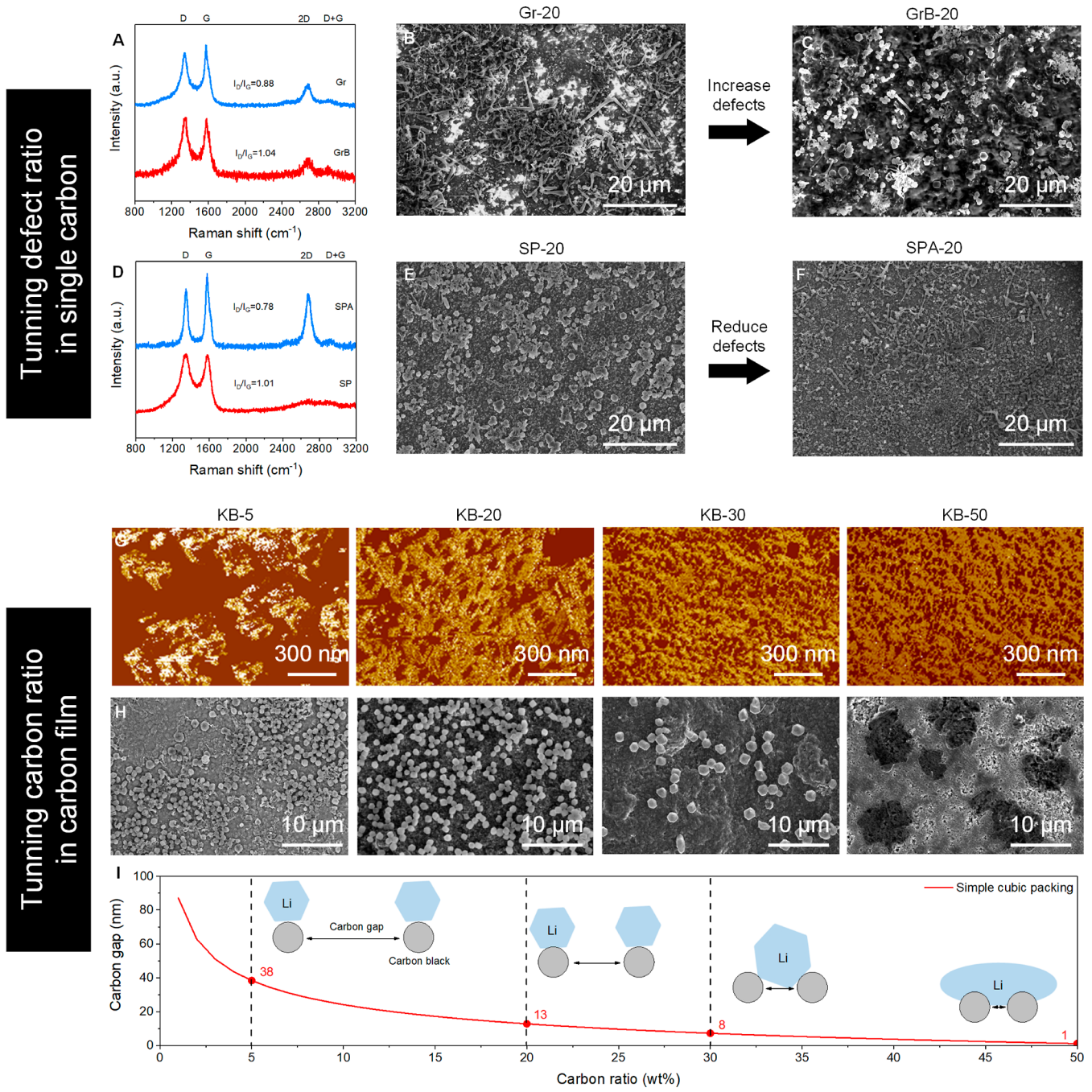

Figure 3. Manipulating the concentration and distribution of carbon defects to control lithium nucleation. (A) Raman spectra of graphene (Gr) before and after ball milling (GrB); (B,C) SEM images of Li seeds on the composite films containing 20% Gr (Gr-20) and GrB (GrB-20); (D) Raman spectra of Super P (SP) before and after annealing (SPA); (E,F) SEM images of Li seeds on the composite films containing 20% SP (SP-20) and SPA (SPA-20); (G) C-AFM images of KB-5, KB-20, KB-30, and KB-50; (H) SEM images of Li deposited on films in (G). (I) Gap between carbon particles as a function of carbon loading which leads to different lithium nucleation behavior as depicted by the schematic diagram. Lithium is deposited at a constant current of 3 mA cm^{-2} and a capacity of 0.1 mA h cm^{-2}.

ratio of 20 wt %. Figure S8 provides top-view scanning electron microscopy (SEM) images of the films, demonstrating the uniform distribution of carbon particles. Carbon typically exhibits an electronic resistivity of around 1×10^{-3} Ω m. The thickness of carbon-polymer films is approximately 3 μm, resulting in an area-specific resistance (ASR) on the order of 10^{-5} Ω cm^2 for a composite containing 5−20% of carbon, which is negligible as compared to the electrode ASR of typical lithium-ion batteries (10s Ω cm^2).[22] Therefore, we anticipate minimal impact from the carbon-polymer coating on the internal resistance within the battery.

To explore the influence of carbon on the nucleation and initial growth of Li, we conduct an experiment in which 0.1 mA h cm^{-2} Li is deposited on films at a current density of 3 mA cm^{-2}. SEM images of the electrodeposited Li on the films are presented in Figure 2B. The morphology of the electrodeposited Li varies significantly across the films. On G-20 and Gr-20 films, Li shows a mixture of dendritic and hexagonal shapes with different sizes. However, on SP-20, KB-20, and

https://doi.org/10.1021/acsnano.4c03498
ACS Nano XXXX, XXX, XXX−XXX

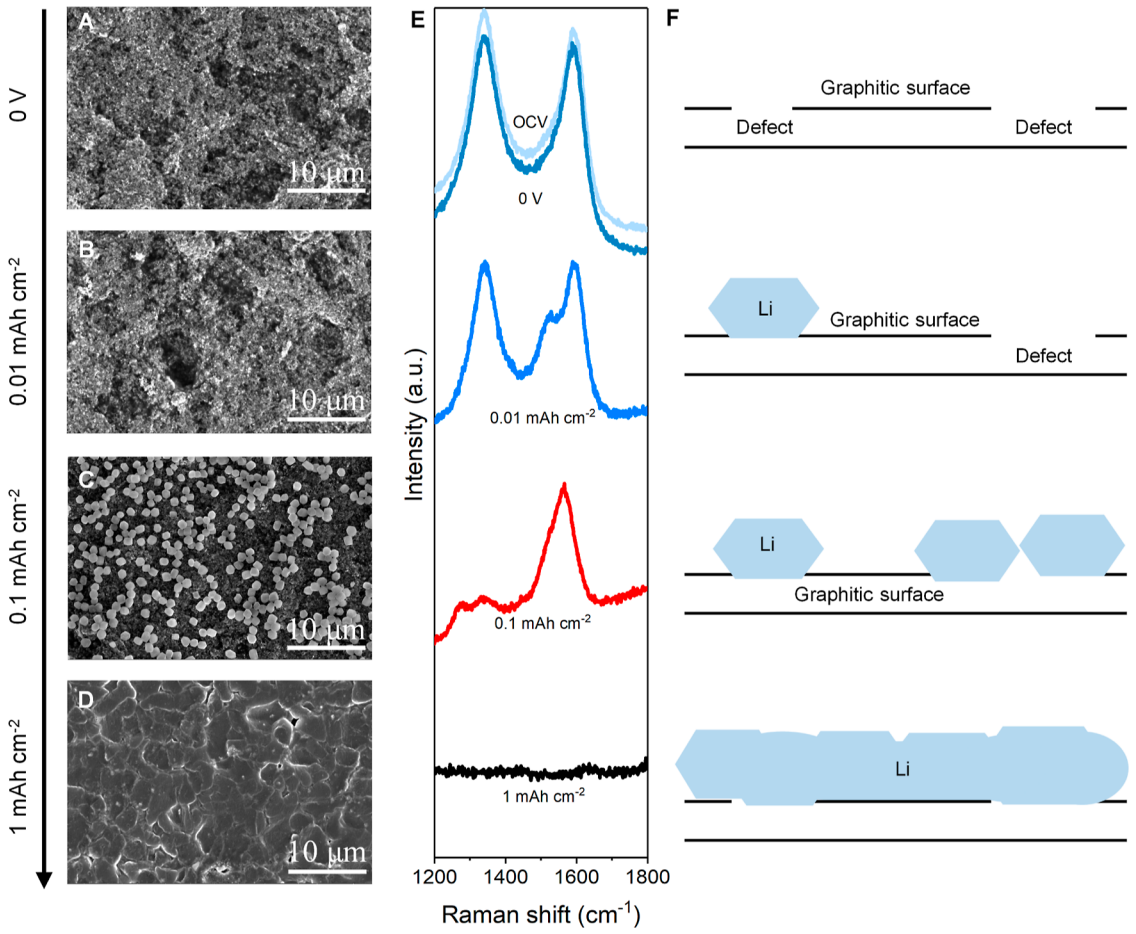

Figure 4. Confirming lithium nucleation on carbon defects. (A–D) SEM images of lithium deposition on KB-20 at different capacities. (E) Ex situ Raman spectra of KB-20 at different stages of lithium deposition. OCV: open circuit voltage; 0 V: biased at 0 V before lithium deposition. (F) Schematic diagram of lithium nucleation and growth on carbon-based substrates. Lithium is deposited at a constant current of 3 mA cm^{-2}.

CNT-20 films, Li shapes consist of relatively uniform hexagons. To quantitatively assess the morphological differences, we measure the sizes of approximately 100 Li particles and plot the distribution in Figure 2C. The median sizes of Li particles across all five films are similar, approximately 2 μm (Figure S9). However, they display a significant disparity in terms of the standard deviation (SD). The SD values for G-20, Gr-20, SP-20, KB-20, and CNT-20 are 4.68, 3.34, 1.02, 0.15, and 0.24 μm, respectively. Films with higher I_D/I_G ratios show greater uniformity (lower SD) in Li size. Furthermore, a comprehensive analysis is conducted to explore the influence of other factors on the uniformity (SD) of Li seed size, yet most of them display a low correlation. It is widely accepted that lithium prefers depositing on lithiophilic substrates.[23] Interestingly, Li nucleates as faceted crystals on KB (with a molten Li contact angle of 140°), while dendrites form on graphite (with a molten Li contact angle of 70°; Figure S5). Increasing the surface area of the substrate is generally believed to benefit lithium plating by reducing local current density.[24] However, the SD of Li seed size on Gr (with a surface area of 750 m^2 g^{-1}) is three times larger than the SD of Li seed size on SP (with a surface area of 88 m^2 g^{-1}, Figure S6). Some studies suggest that amorphous carbon is more favorable for metal plating than graphitic carbon.[25] Surprisingly, similar and uniform faceted Li seeds occur on both KB (amorphous carbon) and CNT (graphitic carbon; Figure S7). We also carefully check the lithiation capacities of carbon and the nucleation overpotentials of Li on the films (Figure S10), yet they demonstrate a low correlation with the SD of Li seed size. Among all the variables, the I_D/I_G ratio exhibits the highest coefficient of correlation with the uniformity of Li seed size (Figure S11), suggesting that the defect density of carbon rather than its ability to intercalate or wet lithium drives the nucleation behavior. These findings support our hypothesis that carbon defects play a crucial role in Li nucleation and initial Li deposition.

Tuning Defect Density and Distribution to Control Li Nucleation. To gain deeper insights into the effect of carbon defects on Li nucleation and initial deposition, we designed three additional experiments seeking to manipulate the density and distribution of defects. The first strategy involves ball milling, a traditional method known for increasing the defect concentration in carbon particles.[26−28] Here, we subject Gr particles to 1 h of ball milling, resulting in an increase in the I_D/I_G ratio from 0.88 to 1.04 (GrB, Figure 3A). As expected, the uniformity of Li seed deposition on GrB-20 significantly improved, with the standard deviation (SD) decreasing from 3.34 to 0.95, along with a notable reduction in dendrite-like Li structures (Figure 3B,C). Next, we employ high-temperature annealing as the second strategy to reduce the concentration of carbon defects on carbon particles.[29−31] SP particles are annealed at 2000 °C for 2 h under flowing argon, leading to a

https://doi.org/10.1021/acsnano.4c03498
ACS Nano XXXX, XXX, XXX−XXX

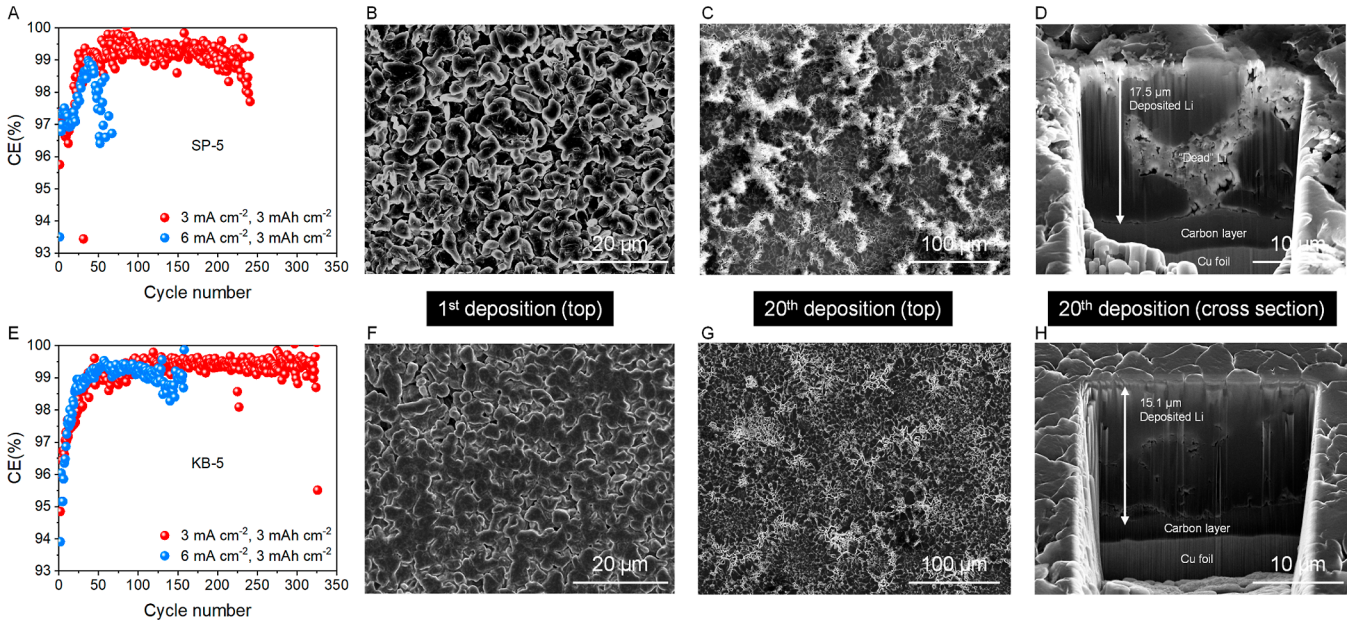

Figure 5. Substrate effects on cycle life of half cells. CE as a function of cycle number on SP-5 (A) and KB-5 (E) at two different current densities; top view SEM images of Li after 1st deposition and after 20th deposition: (B,C), SP-5; (F,G), KB-5; and cross-sectional SEM images of lithium after 20th deposition: (D), SP-5 and (H), KB-5.

decrease in the I_D/I_G ratio from 1.01 to 0.78 (SPA, Figure 3D). Interestingly, the uniformity of Li seed deposition on SPA-20 deteriorated, as evidenced by an increase in the SD from 1.02 to 2.62. There is also the appearance of dendrite-like Li structures (Figure 3E,F). These results collectively demonstrate the significant role played by the concentration of carbon defects on the substrates in guiding Li nucleation and the initial deposition process. The strategies of ball milling and annealing provide valuable insights into the impact of carbon defects on Li electrodeposition.

Furthermore, we investigate the influence of the gap between carbon particles by adjusting the carbon ratio in KB-W films (W: 5, 20, 30, and 50). The top-view and cross-sectional SEM images of the KB-W films are presented in Figure S12. KB-5 and KB-20 films exhibit low porosity, resembling dense polymer films. This observation suggests that the substrate's effect on Li nucleation primarily depends on the exposed carbon on the surface layer. However, it is worth noting that PVDF does not completely coat the carbon surface conformally but instead connects the KB particles (Figure S13). Increasing the carbon ratio thus exposes more carbon (including defects) on the surface. To gain further insight into the distribution of carbon defects on the KB-W films, we employ conductive atomic force microscopy (C-AFM) to map the conductivity distribution (Figure 3G). The gold-colored regions represent high electronic conductivity, while the brown-colored regions indicate low electronic conductivity. As the carbon ratio increases from 5 to 50 wt %, the distribution uniformity of carbon improves. Interestingly, the mode of Li deposition changes in KB-30 and KB-50 (Figure 3H). On KB-30, the average size of Li seeds increases from 1.5 to 2 μm. When the carbon ratio reaches 50 wt %, Li deposition prefers to occur as connected planar Li structures rather than growing as individual hexagons on the surface. We posit that variation in the deposition mode is related to the gap between nucleation sites (carbon defects). To investigate the relationship between the gap and deposition mode, we construct a simple structural model of the film, assuming that KB particles pack in an ideal cubic arrangement (Figure 3I). We take carbon and PVDF densities of 2 and 1.76 g cm^{-3}, respectively. Theoretically, the gaps between two KB particles in KB-5, KB-20, KB-30, and KB-50 films are 38, 13, 8, and 1 nm, respectively. In KB-5 and KB-20 films, the gap between two nucleation sites is relatively large (>13 nm), resulting in a significant diffusion barrier for Li atoms and Li clusters. As a consequence, Li tends to locally nucleate as hexagons. At this stage, the size of Li seeds, approximately 1.5 μm, remains independent of the size of the gap. However, when the gap decreases to less than 8 nm, the gap between two nucleation sites begins to affect the mode of Li nucleation. More Li atoms/clusters can merge to form larger hexagons in the earlier stage of seed growth.

Confirmation of Defects as Nucleation Sites. The next question is whether we can directly show if carbon defects indeed serve as nucleation sites. Here, we select KB-20 as the model system to investigate the role of carbon defects during Li nucleation. Li|KB-20 half-cells are discharged to a designed voltage or capacity, and the KB-20 electrodes are then characterized using SEM (Figure 4A–D) and Raman spectroscopy (Figure 4E). The Raman spectra of KB-20 at 0 V and at the open-circuit potential appear similar, and no noticeable SEI formation can be observed through SEM (Figure 4A). After depositing 0.01 mA h cm^{-2} of Li, no distinct Li particles are found (Figure 4B). However, a new Raman peak appears near the G band, which can be attributed to carbon lithiation.[32] Upon depositing 0.1 mA h cm^{-2} Li, uniform Li seeds are observed on the surface of KB-20 (Figure 4C), and the D band disappears while the G band broadens, indicating Li nucleation on carbon defects. After depositing 1 mA h cm^{-2} of Li, the KB-20 surface is covered by a compact layer of Li (Figure 4D), and both the D band and G band have vanished. These findings support our hypothesis that intrinsic defects in pure carbon particles can serve as nucleation sites and that a well-

https://doi.org/10.1021/acsnano.4c03498
ACS Nano XXXX, XXX, XXX−XXX

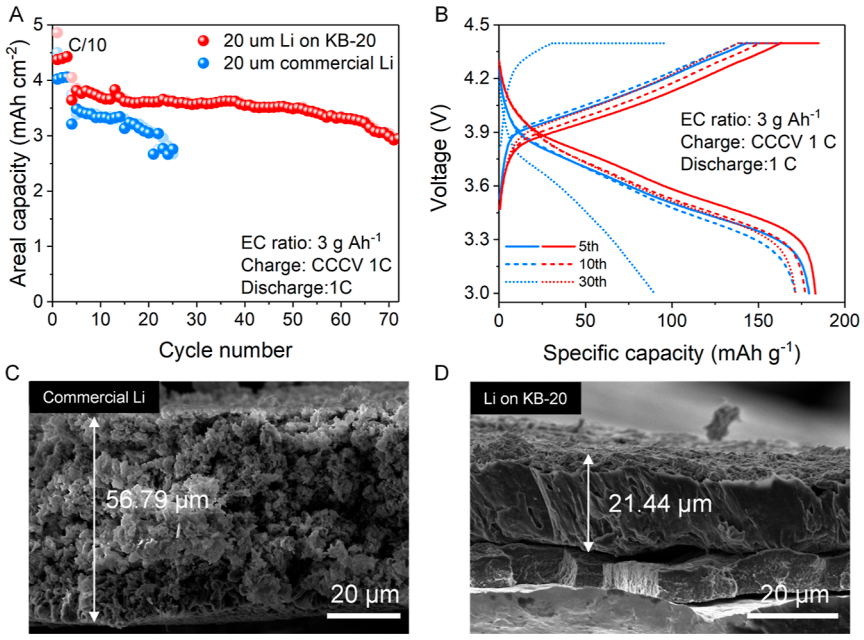

Figure 6. Full cell evaluation in coin cells. (A,B) Capacity retention for two cells with either lithium deposited on KB-20 or a commercial 20 μm Li foil paired with an NMC811 cathode (4 mA h cm^{-2}) and LDME electrolyte (3 g A h^{-1}). Constant current constant voltage cycling is performed at 1 C rate, with the voltage window of 3−4.4 V. The total time of CC and CV is 1 h. Cross-sectional SEM images of (C) commercial Li and (D) Li on KB-20 after 20 cycles.

distributed presence of carbon defects results in uniform Li nucleation (Figures 1 and 4F).

Substrate Effect on the Cycle Life of LMBs. Our findings have demonstrated that surfaces rich in carbon defects facilitate uniform Li nucleation and initial deposition (Figure S14). In theory, a low-porosity morphology should result in superior cycling performance.[3,12] To evaluate this, we examine the CE and cycle life of various substrates, including Cu foil, G-20, Gr-20, SP-5, SP-20, SPA-20, KB-5, KB-20, and CNT-20, at a current density of 3 mA cm^{-2} and an areal capacity of 3 mA h cm^{-2} using the LDME electrolyte (Figures 5 and S15). While all substrates exhibit a similar CE of approximately 99.1%, their cycle life vary from 100 cycles to 300 cycles. As a case study, we focus on SP-5 and KB-5. The CE and cycle life of SP-5 are found to be 99.0% and 241 cycles, respectively, while KB-5 exhibits a CE of 99.2% and a cycle life of 325 cycles (Figure 5A,E). The initial Li morphologies (0.1 mA h cm^{-2}) on these two substrates are dramatically different. SP-5 shows a dendritic Li morphology (Figure S16), while KB-5 exhibits uniform hexagonal Li deposition (Figure 3H). Then we examine the Li morphology after the first electrodeposition of 3 mA h cm^{-2} of Li. Although the individual Li particle morphologies are similar, the porosity of Li on KB-5 (Figure 5F) is lower than that on SP-5 (Figure 5B). Furthermore, the difference in the uniformity of deposited Li between SP-5 and KB-5 becomes more pronounced after 20 cycles. SP-5 exhibits random accumulation of dead Li/SEI between the deposited Li, with a total thickness of 17.5 μm (Figure 5C,D). In contrast, KB-5 maintains a compact Li deposition without noticeable dead Li accumulation with a total thickness of 15.1 μm (Figure 5G,H), which closely matches the ideal thickness of 3 mA h cm^{-2} of Li (14.6 μm). X-ray photoelectron spectroscopy (XPS) analysis of the SEI layers on both electrodes after 20 cycles reveals similar compositions with nearly the same ratios of O, C, N, F, and S (Figure S17). These results indicate that the CE of the Li anode is primarily affected by the SEI (electrolyte), while the cycle life depends on the porosity and uniformity of the deposited Li. To further support this argument, we evaluate Li|SP-5 and Li|KB-5 half-cells at a current density of 6 mA cm^{-2} and an areal capacity of 3 mA h cm^{-2}. The Li|SP-5 cell lasted 50 cycles before failing (Figure 5A). In contrast, the Li|KB-5 cell lasts over 158 cycles, with an average CE exceeding 99% after 20 cycles (Figure 5E). The improvement observed at such a high current density points to the promise for fast charging batteries.

We next investigate the performance of substrates rich in carbon defects in full cells, consisting of an Li-$Ni_{0.8}Mn_{0.1}Co_{0.1}O_2$ (NMC811) cathode with a 4.5 mA h cm^{-2} areal capacity and an anode of either Cu foil or KB-20 film with predeposited Li (4 mA h cm^{-2}), under a lean electrolyte condition of 3 g A h^{-1} (~12 μL per coin cell). This set up corresponds to an N/P ratio of 0.89. Additionally, the NMC811 full cells are cycled at a 1 C rate, corresponding to a current density of approximately 4.5 mA cm^{-2}. Figure 6A illustrates the cycling performance of the full cells. The Cu cell lasts only 20 cycles before experiencing rapid degradation. The cell capacity decays from >3.5 mA h cm^{-2} to approximately 1.2 mA h cm^{-2} within a few cycles. This degradation pattern is similar to that observed in lean-electrolyte cells reported in the literature, which can be attributed to electrolyte depletion.[3] In contrast, the KB-20 cell demonstrates stable cycling for 60 cycles until all predeposited Li is depleted, after which it maintains a CE of ~99.2%. The voltage profile, as shown in Figure 6B, also indicates that the presence of KB-20 leads to a slower evolution of the Li anode impedance. To gain insights into the underlying mechanisms for the significant difference in cyclability, the cells are disassembled after 20 cycles to examine the morphology of Li. On the KB-20 substrate, the Li maintains a compact structure (Figure 6D). In contrast, Li on Cu exhibits an extremely porous and mossy morphology (Figure 6C). The Li layer thickness on KB-20 is 21.44 μm including ~2 μm thick SEI/dead Li layer on the top surface,

https://doi.org/10.1021/acsnano.4c03498
ACS Nano XXXX, XXX, XXX−XXX

while on Cu it is 56.79 μm. These findings are consistent with the evaluations conducted in half-cells (Figure 5D,H), indicating that the substrate effect persists, even under full cell conditions. The cycle life demonstrated by the full cell with the Li anode formed from faceted Li seeds is among the best reported so far, especially when considering the low E/C ratio and the high rates of cycling such as 1 C (Table S2). The carbon composite film is fabricated using the standard blade coating process, which is compatible with current battery manufacturing infrastructure. Although prelithiation is currently necessary for practical implementations of the film in a full cell, continued progress in prelithiation is likely to bring it closer to reality.

CONCLUSIONS

We have shown that carbon-polymer films can serve as substrates for promoting the deposition of faceted Li crystals with hexagonal shape. We demonstrate that the intrinsic defects present in pure carbon particles can effectively serve as nucleation sites for Li. Notably, we find that when the I_D/I_G ratio of carbon exceeds 1 and the interparticle gap falls within the range of 8−38 nm, lithium exhibits a preference for depositing as hexagonal Li seeds. These crystalline Li seeds play a crucial role in facilitating low-porosity Li deposition, mitigating Li pulverization during cycling, and unlocking the fast-charging ability of Li metal batteries. We have achieved a 313% improvement in cycle life compared with baseline cells under a 1 C rate. Our understanding of the role of intrinsic carbon defects on Li nucleation provides valuable insights for designing substrates suitable for high-energy-density LMBs capable of fast charging. The carbon films are low-cost and easy to fabricate, making it feasible to scale up this technology for large-scale applications.

METHODS

Chemicals. Lithium foil (100 μm), graphene, ketjen black (KB, EC600JD), and PVDF binder were ordered from MSE Supplies. Super P carbon was received from TIMCAL. Graphite was received from Xiamen Knano Graphene Technology Co. $LiNi_{0.8}Mn_{0.1}Co_{0.1}O_2$ (NMC811) powders were purchased from Targray Technology International Inc. Lithium bis(fluorosulfonyl)imide (LiFSI) and 1,2-dimethoxyethane (DME) were purchased from Gotion. Bis(2,2,2-trifluoroethyl)ether (BTFE) was purchased from TCI. Electrolytes were prepared by dissolving predetermined amounts of LiFSI salt into the solvents of interest and stirred.

Carbon-Polymer Film Preparation. The carbon-polymer film was fabricated by a slurry casting method. Initially, carbon and PVDF were ground together in specified weight ratios by using a mortar and pestle. The resulting mixture was then dispersed in *N*-methyl pyrrolidone (NMP, Sigma-Aldrich) using a Thinky Mixer, operating at 2000 rpm for 1 h. Subsequently, the obtained slurry was cast onto a copper foil (9 μm, MTI) by using a film casting doctor blade and an automatic film coater (MSK-AFA-III). Lastly, the film was subjected to vacuum drying at 110 °C for a duration of 12 h.

Carbon Annealing. Carbon powders were placed in a high purity graphite crucible (SPEX, USA) and subsequently annealed in an RD Webb "Red Devil" furnace (MA, USA) at 2000 °C for 2 h under flowing argon. The furnace was pumped down to a rough vacuum (10^{-2} to 10^{-3} mbar) overnight to evacuate as much oxygen from the hot zone and carbon powder sample as possible prior to the annealing step. A heating rate of 25 °C min^{-1} was employed until 1500 °C. After a 30 min soak to stabilize the temperature in the hot zone, the temperature was increased to 2000 °C at a rate of 10 °C min^{-1} and held for 2 h. The sample was subsequently furnace cooled at the end of the annealing cycle.

Cathode Preparation. The NMC811 electrode was prepared by coating a slurry composed of NMC811 powder, Super P, and PVDF binder in a ratio of 90:5:5 wt % with NMP as the solvent on a carbon coated aluminum foil. The coated electrode was vacuum-dried at 110 °C. The cathode active material loading is around 22 mg cm^{-2}.

Electrochemical Test. 2032-type coin cells were used for all of the electrochemical studies in this work. The Li foil (100 μm) was punched into 12 mm discs as the counter electrode. Celgar2325 was used as the separator. The carbon substrates were punched into 14 mm discs as the working electrodes. A fixed amount of electrolyte (50 μL) was added to each cell. Lithium deposition and galvanostatic cycling was conducted on a Land battery tester.

For NMC811 coin cell tests, the commercial Li foil (20 μm) and KB-20 (a carbon-polymer composite film, the weight ratio of KB/PVDF is 1:4, with 4 mA h cm^{-2} Li) were punched to 15 mm discs and used as the anode; the NMC811 electrode was punched to 14 mm discs and used as the cathode. Celgard 2325 was used as the separator. NMC811 coin cells were constructed with an electrolyte/capacity ratio of 3 g A h^{-1}. The cells were cycled at a C/10 rate for 3 cycles and then tested under predetermined rates (1 C = 200 mA g^{-1}). Galvanostatic charge−discharge cycling was conducted between 3 and 4.4 V on a Land battery tester.

X-ray Photoelectron Spectroscopy. The XPS results were obtained on an AXIS Supra XPS instrument by Kratos Analytical. XPS spectra were collected by using a monochromatized Al Kα source (1486.7 eV). Samples were characterized under 10^{-8} Torr of vacuum. The cycled electrode was recovered by disassembling the coin cell. All of the samples were washed with DME three times and dried in the glovebox antechamber under vacuum. All samples were transferred from a nitrogen filled glovebox, which was directly connected to XPS. A 10 keV Ar (1000 atom) cluster source was applied for 60 s etching. All XPS spectra were calibrated with adventitious C 1s (284.8 eV) and analyzed using the CasaXPS software.

Scanning Electron Microscopy. The SEM images of lithium were obtained on SEM (FEI Apreo). The cycled electrode was recovered by disassembling the coin cell. All the samples were washed with DME three times and dried in the glovebox antechamber under vacuum. The sample was adhered to double-sided carbon tape and placed on a specimen holder. The prepared sample was sealed in a glass bottle inside the glovebox for transferring to the SEM. The approximate time of the sample exposed to air (from a sealed environment to the SEM stage) was less than 3 s.

ASSOCIATED CONTENT

Supporting Information

The Supporting Information is available free of charge at https://pubs.acs.org/doi/10.1021/acsnano.4c03498.

SEM images of Li nuclei on different substrates, SEM, TEM images, and EDS mapping of carbon materials, optical images of molten Li on carbon; particle size, surface area, XRD patterns, and *fwhm* of carbon materials; medium size and standard deviation of Li seed size; capacity−voltage curves for lithiation of carbon materials; correlation analysis of Li seed size with materials properties; CE of Li cycling; XPS analysis of carbon films; table of true density of carbon particles; and table of performance comparison for LMBs (PDF)

AUTHOR INFORMATION

Corresponding Author

Ping Liu − *Program of Materials Science and Engineering, University of California, San Diego, La Jolla, California 92093, United States; Sustainable Power and Energy Center, Aiiso Yufeng Li Family Department of Chemical and Nano Engineering, and Program of Chemical Engineering, University of California, San Diego, La Jolla, California*

https://doi.org/10.1021/acsnano.4c03498
ACS Nano XXXX, XXX, XXX−XXX

92093, United States; orcid.org/0000-0002-1488-1668; Email: piliu@ucsd.edu

Authors

Sicen Yu – *Program of Materials Science and Engineering, University of California, San Diego, La Jolla, California 92093, United States; Sustainable Power and Energy Center, University of California, San Diego, La Jolla, California 92093, United States;* orcid.org/0000-0001-6456-1155

Xiaolu Yu – *Program of Materials Science and Engineering, University of California, San Diego, La Jolla, California 92093, United States; Sustainable Power and Energy Center, University of California, San Diego, La Jolla, California 92093, United States*

Sashank Shivakumar – *Program of Materials Science and Engineering, University of California, San Diego, La Jolla, California 92093, United States; Aiiso Yufeng Li Family Department of Chemical and Nano Engineering, University of California, San Diego, La Jolla, California 92093, United States;* orcid.org/0000-0002-9859-3048

Shen Wang – *Sustainable Power and Energy Center and Aiiso Yufeng Li Family Department of Chemical and Nano Engineering, University of California, San Diego, La Jolla, California 92093, United States*

Erbin Qiu – *Department of Physics, University of California, San Diego, La Jolla, California 92093, United States;* orcid.org/0000-0001-7446-9248

Qiushi Miao – *Program of Materials Science and Engineering, University of California, San Diego, La Jolla, California 92093, United States; Sustainable Power and Energy Center, University of California, San Diego, La Jolla, California 92093, United States;* orcid.org/0009-0008-0857-6107

Junwei Gao – *Program of Materials Science and Engineering, University of California, San Diego, La Jolla, California 92093, United States*

Min Wei – *Tyfast Energy Corp, La Jolla, California 92093, United States*

Jianbin Zhou – *Sustainable Power and Energy Center and Aiiso Yufeng Li Family Department of Chemical and Nano Engineering, University of California, San Diego, La Jolla, California 92093, United States*

Zheng Chen – *Program of Materials Science and Engineering, University of California, San Diego, La Jolla, California 92093, United States; Sustainable Power and Energy Center, University of California, San Diego, La Jolla, California 92093, United States;* orcid.org/0000-0002-9186-4298

Complete contact information is available at: https://pubs.acs.org/10.1021/acsnano.4c03498

Author Contributions

P. Liu supervised the project. S. Yu and P. Liu designed the experiments. S. Yu carried out electrochemical tests and data analysis. S. Yu and J. Zhou conducted SEM tests. X. Yu and Z. Chen carried out TEM tests. S. Shivakumar assisted with carbon annealing experiments. S. Wang and Q. Miao conducted Raman tests. S. Wang carried out cryo-FIB. E. Qiu, M. Wei, and J. Gao assisted with cell assembly. S. Yu and P. Liu wrote the manuscript. All authors commented on the final manuscript.

Notes

The authors declare the following competing financial interest(s): A patent disclosure is filed with University of California San Diego's Office of Innovation and Commercialization.

ACKNOWLEDGMENTS

This work was performed in part at the San Diego Nanotechnology Infrastructure (SDNI) of University of California San Diego, a member of the National Nanotechnology Coordinated Infrastructure (NNCI), which is supported by the National Science Foundation (grant ECCS-1542148). This work was supported by the Office of Vehicle Technologies of the U.S. Department of Energy through the Advanced Battery Materials Research (BMR) Program (Battery500 Consortium) under Contract PNNL-595241 to P.L. We acknowledge the support from J. Luo at the University of California San Diego for helping us with carbon annealing.

REFERENCES

(1) Armand, M.; Tarascon, J.-M. Building better batteries. *Nature* **2008**, *451*, 652–657.

(2) Liu, J.; Bao, Z.; Cui, Y.; Dufek, E. J.; Goodenough, J. B.; Khalifah, P.; Li, Q.; Liaw, B. Y.; Liu, P.; Manthiram, A.; et al. Pathways for practical high-energy long-cycling lithium metal batteries. *Nat. Energy* **2019**, *4*, 180–186.

(3) Wu, Z.; Wang, C.; Hui, Z.; Liu, H.; Wang, S.; Yu, S.; Xing, X.; Holoubek, J.; Miao, Q.; Xin, H. L.; et al. Growing single-crystalline seeds on lithiophobic substrates to enable fast-charging lithium-metal batteries. *Nat. Energy* **2023**, *8*, 340–350.

(4) Niu, C.; Lee, H.; Chen, S.; Li, Q.; Du, J.; Xu, W.; Zhang, J.-G.; Whittingham, M. S.; Xiao, J.; Liu, J. High-energy lithium metal pouch cells with limited anode swelling and long stable cycles. *Nat. Energy* **2019**, *4*, 551–559.

(5) Fan, X.; Wang, C. High-voltage liquid electrolytes for Li batteries: progress and perspectives. *Chem. Soc. Rev.* **2021**, *50*, 10486–10566.

(6) Liu, H.; Holoubek, J.; Zhou, H.; Chen, A.; Chang, N.; Wu, Z.; Yu, S.; Yan, Q.; Xing, X.; Li, Y.; et al. Ultrahigh coulombic efficiency electrolyte enables Li|| SPAN batteries with superior cycling performance. *Mater. Today* **2021**, *42*, 17–28.

(7) Weber, R.; Genovese, M.; Louli, A.; Hames, S.; Martin, C.; Hill, I. G.; Dahn, J. Long cycle life and dendrite-free lithium morphology in anode-free lithium pouch cells enabled by a dual-salt liquid electrolyte. *Nat. Energy* **2019**, *4*, 683–689.

(8) Niu, C.; Liu, D.; Lochala, J. A.; Anderson, C. S.; Cao, X.; Gross, M. E.; Xu, W.; Zhang, J.-G.; Whittingham, M. S.; Xiao, J.; et al. Balancing interfacial reactions to achieve long cycle life in high-energy lithium metal batteries. *Nat. Energy* **2021**, *6*, 723–732.

(9) Hobold, G. M.; Lopez, J.; Guo, R.; Minafra, N.; Banerjee, A.; Shirley Meng, Y.; Shao-Horn, Y.; Gallant, B. M. Moving beyond 99.9% Coulombic efficiency for lithium anodes in liquid electrolytes. *Nat. Energy* **2021**, *6*, 951–960.

(10) Shang, Y.; Chu, T.; Shi, B.; Fu, K. Scalable Synthesis of LiF-rich 3D Architected Li Metal Anode via Direct Lithium-Fluoropolymer Pyrolysis to Enable Fast Li Cycling. *Energy Environ. Mater.* **2021**, *4*, 213–221.

(11) Li, Q.; Zhu, S.; Lu, Y. 3D Porous Cu Current Collector/Li-Metal Composite Anode for Stable Lithium-Metal Batteries. *Adv. Funct. Mater.* **2017**, *27*, 1606422.

(12) Fang, C.; Lu, B.; Pawar, G.; Zhang, M.; Cheng, D.; Chen, S.; Ceja, M.; Doux, J.-M.; Musrock, H.; Cai, M.; et al. Pressure-tailored lithium deposition and dissolution in lithium metal batteries. *Nat. Energy* **2021**, *6*, 987–994.

(13) Louli, A.; Eldesoky, A.; Weber, R.; Genovese, M.; Coon, M.; deGooyer, J.; Deng, Z.; White, R.; Lee, J.; Rodgers, T.; et al. Diagnosing and correcting anode-free cell failure via electrolyte and morphological analysis. *Nat. Energy* **2020**, *5*, 693–702.

(14) Boyle, D. T.; Li, Y.; Pei, A.; Vilá, R. A.; Zhang, Z.; Sayavong, P.; Kim, M. S.; Huang, W.; Wang, H.; Liu, Y.; et al. Resolving Current-

Dependent Regimes of Electroplating Mechanisms for Fast Charging Lithium Metal Anodes. *Nano Lett.* **2022**, *22*, 8224−8232.
(15) Yuan, X.; Liu, B.; Mecklenburg, M.; Li, Y. Ultrafast deposition of faceted lithium polyhedra by outpacing SEI formation. *Nature* **2023**, *620*, 86−91.
(16) Liu, S.; Zhang, X.; Li, R.; Gao, L.; Luo, J. Dendrite-free Li metal anode by lowering deposition interface energy with Cu99Zn alloy coating. *Energy Storage Mater.* **2018**, *14*, 143−148.
(17) Yu, S.; Wu, Z.; Holoubek, J.; Liu, H.; Hopkins, E.; Xiao, Y.; Xing, X.; Lee, M. H.; Liu, P. A Fiber-Based 3D Lithium Host for Lean Electrolyte Lithium Metal Batteries. *Adv. Sci.* **2022**, *9*, 2104829.
(18) Hagopian, A.; Doublet, M.-L.; Filhol, J.-S. Thermodynamic origin of dendrite growth in metal anode batteries. *Energy Environ. Sci.* **2020**, *13*, 5186−5197.
(19) Childres, I.; Jauregui, L. A.; Park, W.; Cao, H.; Chen, Y. P. Raman spectroscopy of graphene and related materials. *New Developments in Photon and Materials Research*; Nova Publishers, 2013; Vol. *1*, pp 1−20.
(20) Xue, D.; Xia, H.; Yan, W.; Zhang, J.; Mu, S. Defect engineering on carbon-based catalysts for electrocatalytic CO_2 reduction. *Nano-Micro Lett.* **2021**, *13*, 5−23.
(21) Jiang, Y.; Yang, L.; Sun, T.; Zhao, J.; Lyu, Z.; Zhuo, O.; Wang, X.; Wu, Q.; Ma, J.; Hu, Z. Significant contribution of intrinsic carbon defects to oxygen reduction activity. *ACS Catal.* **2015**, *5*, 6707−6712.
(22) Kubal, J. J.; Knehr, K. W.; Susarla, N.; Tornheim, A.; Dunlop, A. R.; Dees, D. D.; Jansen, A. N.; Ahmed, S. The influence of temperature on area-specific impedance and capacity of Li-ion cells with nickel-containing positive electrodes. *J. Power Sources* **2022**, *543*, 231864.
(23) Yan, K.; Lu, Z.; Lee, H.-W.; Xiong, F.; Hsu, P.-C.; Li, Y.; Zhao, J.; Chu, S.; Cui, Y. Selective deposition and stable encapsulation of lithium through heterogeneous seeded growth. *Nat. Energy* **2016**, *1*, 16010.
(24) Yang, C. P.; Yin, Y. X.; Zhang, S. F.; Li, N. W.; Guo, Y. G. Accommodating lithium into 3D current collectors with a submicron skeleton towards long-life lithium metal anodes. *Nat. Commun.* **2015**, *6*, 8058.
(25) Li, Y.; Zhou, Q.; Weng, S.; Ding, F.; Qi, X.; Lu, J.; Li, Y.; Zhang, X.; Rong, X.; Lu, Y.; et al. Interfacial engineering to achieve an energy density of over 200 Wh kg^{-1} in sodium batteries. *Nat. Energy* **2022**, *7*, 511−519.
(26) Dong, Y.; Zhang, S.; Du, X.; Hong, S.; Zhao, S.; Chen, Y.; Chen, X.; Song, H. Boosting the electrical double-layer capacitance of graphene by self-doped defects through ball-milling. *Adv. Funct. Mater.* **2019**, *29*, 1901127.
(27) Yuan, R.; Dong, Y.; Hou, R.; Shang, L.; Zhang, J.; Zhang, S.; Chen, X.; Song, H. Structural transformation of porous and disordered carbon during ball-milling. *Chem. Eng. J.* **2023**, *454*, 140418.
(28) Lu, H.; Ai, F.; Jia, Y.; Tang, C.; Zhang, X.; Huang, Y.; Yang, H.; Cao, Y. Exploring sodium-ion storage mechanism in hard carbons with different microstructure prepared by ball-milling method. *Small* **2018**, *14*, 1802694.
(29) Behler, K.; Osswald, S.; Ye, H.; Dimovski, S.; Gogotsi, Y. Effect of thermal treatment on the structure of multi-walled carbon nanotubes. *J. Nanopart. Res.* **2006**, *8*, 615−625.
(30) Xu, Z.; Guo, Z.; Madhu, R.; Xie, F.; Chen, R.; Wang, J.; Tebyetekerwa, M.; Hu, Y.-S.; Titirici, M.-M. Homogenous metallic deposition regulated by defect-rich skeletons for sodium metal batteries. *Energy Environ. Sci.* **2021**, *14*, 6381−6393.
(31) Yoon, H. J.; Kim, N. R.; Jin, H. J.; Yun, Y. S. Macroporous catalytic carbon nanotemplates for sodium metal anodes. *Adv. Energy Mater.* **2018**, *8*, 1701261.
(32) Cheng, X.-q.; Li, H.-j.; Zhao, Z.-x.; Wang, Y.-z.; Wang, X.-m. The use of in-situ Raman spectroscopy in investigating carbon materials as anodes of alkali metal-ion batteries. *New Carbon Mater.* **2021**, *36*, 93−105.

https://doi.org/10.1021/acsnano.4c03498
ACS Nano XXXX, XXX, XXX−XXX